



## RESEARCH ARTICLE

# Wide-field Stokes polarimetric microscopy for second harmonic generation imaging

Leonardo Uribe Castaño<sup>1,2</sup>  | Kamdin Mirsanaye<sup>1,2</sup> | Lukas Kontenis<sup>3,4</sup> |  
Serguei Krouglov<sup>1,2</sup> | Edvardas Žurauskas<sup>5</sup> | Roya Navab<sup>6</sup> |  
Kazuhiro Yasufuku<sup>6,7</sup> | Ming-Sound Tsao<sup>6</sup> | Margarete K. Akens<sup>8,9,10</sup> |  
Brian C. Wilson<sup>6,8</sup>  | Virginijus Barzda<sup>1,2,3</sup>

<sup>1</sup>Department of Physics, University of Toronto, Toronto, Ontario, Canada

<sup>2</sup>Department of Chemical and Physical Sciences, University of Toronto Mississauga, Mississauga, Ontario, Canada

<sup>3</sup>Laser Research Centre, Faculty of Physics, Vilnius University, Vilnius, Lithuania

<sup>4</sup>Light Conversion, Vilnius, Lithuania

<sup>5</sup>Department of Pathology, Forensic Medicine and Pharmacology, Vilnius University, Vilnius, Lithuania

<sup>6</sup>Princess Margaret Cancer Centre, University Health Network, Toronto, Ontario, Canada

<sup>7</sup>Toronto General Hospital, University Health Network, Toronto, Ontario, Canada

<sup>8</sup>Department of Medical Biophysics, University of Toronto, Toronto, Ontario, Canada

<sup>9</sup>Techna Institute, University Health Network, Toronto, Ontario, Canada

<sup>10</sup>Department of Surgery, University of Toronto, Toronto, Ontario, Canada

## Correspondence

Virginijus Barzda, Department of Chemical and Physical Sciences, University of Toronto Mississauga, 3359 Mississauga Rd. North, Mississauga, ON L5L 1C6, Canada.

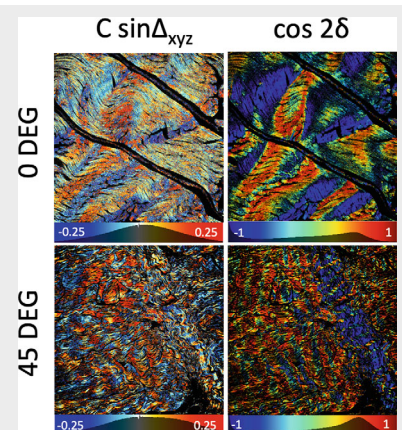
Email: [virgis.barzda@utoronto.ca](mailto:virgis.barzda@utoronto.ca)

## Funding information

European Regional Development Fund, Grant/Award Number: 01.2.2.-LMT-K-718-02-0016; Natural Sciences and Engineering Research Council of Canada, Grant/Award Numbers: DGDND-2017-00099, RGPIN-2017-06923

## Abstract

We employ wide-field second harmonic generation (SHG) microscopy together with nonlinear Stokes polarimetry for quick ultrastructural investigation of large sample areas ( $700 \mu\text{m} \times 700 \mu\text{m}$ ) in thin histology sections. The Stokes vector components for SHG are obtained from the polarimetric measurements with incident and outgoing linear and circular polarization states. The Stokes components are used to construct the images of polarimetric parameters and deduce the maps of ultrastructural parameters of achiral and chiral nonlinear susceptibility tensor components ratios and cylindrical axis orientation in fibrillar materials. The large area imaging was employed for lung tumor margin investigations. The imaging shows reduced SHG intensity, increased achiral susceptibility ratio values, and preferential orientation of collagen strands along the boarder of tumor margin. The wide-field Stokes polarimetric SHG microscopy



This is an open access article under the terms of the [Creative Commons Attribution-NonCommercial](https://creativecommons.org/licenses/by-nc/4.0/) License, which permits use, distribution and reproduction in any medium, provided the original work is properly cited and is not used for commercial purposes.

© 2023 The Authors. *Journal of Biophotonics* published by Wiley-VCH GmbH.

opens a possibility of quick large area imaging of ultrastructural parameters of tissue collagen, which can be used for nonlinear histopathology investigations.

#### KEYWORDS

lung tumor margin imaging, nonlinear optical polarimetry, second harmonic generation microscopy, second-order susceptibility, wide-field microscopy

## 1 | INTRODUCTION

Polarimetric second harmonic generation (SHG) microscopy can be used for ultrastructural characterization of noncentrosymmetric materials [1–5]. It is conveniently applied for investigation of collagen structure in the histology samples [6–9]. For digital histopathology, a large area imaging is necessary, which is a limiting factor when laser scanning microscopy of SHG is employed. In contrast, the wide-field microscopy provides fast imaging of a large area due to parallel detection of the signal onto a pixel array of a camera [10–17]. Video rate imaging can be readily performed with a wide-field nonlinear microscope [18].

The SHG intensity and its polarization sensitivity can be utilized to infer details about collagen organization in the tissue by using polarimetric SHG microscopy techniques (P-SHG) [19–21]. Collagen ultrastructure is altered during tumorigenesis. Therefore, SHG polarimetric and ultrastructure parameters can be employed as biomarkers for cancer diagnostics [22–34]. Full and reduced polarimetry can be applied to deduce the susceptibility tensor component values that characterize the ultrastructure of collagen. Stokes polarimetric parameters can be employed with linear and circular incident and outgoing polarization states in reduced polarimetry measurements to deduce the achiral and chiral molecular second-order susceptibility tensor component ratios ( $R = \chi'_{zzz}/\chi'_{zzx}$ ) and ( $C = \chi'_{xyz}/\chi'_{zxx}$ ), respectively, where prime signifies the susceptibility tensor of fiber projected onto the image plane with  $z$  along the projected fiber axis and  $y$  along the light propagation direction (normal to the image plane) [35–40].

In this work, a wide-field polarimetric SHG microscopy is used to obtain a number of polarimetric parameters including SHG linear dichroism (SHG<sub>LD</sub>), linear anisotropy of linear dichroism (LA<sub>LD</sub>) and circular anisotropy of linear dichroism (CA<sub>LD</sub>), as well as SHG circular dichroism (SHG<sub>CD</sub>), linear anisotropy of circular dichroism (LA<sub>CD</sub>), and circular anisotropy of circular dichroism (CA<sub>CD</sub>). The polarimetric parameters are obtained from Stokes vector components of SHG signal. The parameters then are used to calculate (without fitting) the ultrastructural parameters including achiral and chiral nonlinear susceptibility tensor components ratios  $R$  and  $C$ , and fiber orientation angles in the image plane,  $\delta$ . Direct calculations without fitting of polarization data minimizes the postprocessing

time by more than an order of magnitude, which is essential for large area imaging in digital pathology. The wide-field SHG Stokes polarimetry is applied for rat tail tendon structural investigations and lung tumor margin histopathology. The new wide-field Stokes polarimetric SHG imaging method enables large area mapping of ultrastructural parameters that can be readily applied for nonlinear digital pathology investigations.

## 2 | THEORETICAL CONSIDERATIONS

### 2.1 | Nonlinear Stokes–Mueller formalism for calculating outgoing Stokes vector elements

Linear and circular polarization states can be utilized for incident light as well as to probe the polarization states of generated second harmonic signal. The polarimetric parameters are deduced using double Stokes–Mueller formalism:

$$s = MS, \quad (1)$$

where  $s$  is the four element Stokes vector ( $s_0, s_1, s_2, s_3$ )<sup>t</sup> of generated SHG signal and  $S$  is the nine element double Stokes vector for degenerate two-photon polarization state of laser radiation [41]. The double Mueller matrix  $M$  has  $4 \times 9$  elements. The double Muler matrix components are related to the nonlinear susceptibility tensor components  $\chi_{IJK}^{(2)}$  in the laboratory reference frame (see explicit relations in [42]). In turn, the laboratory reference frame susceptibility components are related to the molecular susceptibility tensor components  $\chi_{ijk}^{(2)}$  via rotation matrix with in-image-plane orientation angle  $\delta$  and out-of-image-plane tilt angle  $\alpha$  of cylindrical structures with C6 symmetry representing collagen fibers. The model of chiral fibrillar aggregate is assumed, where the achiral molecular susceptibilities are real, indicating that there is no phase retardancy between the achiral susceptibility components, but the chiral molecular susceptibility is complex valued having a relative phase retardancy  $\Delta_{xyz}$  between achiral and chiral susceptibility components [38]. The  $R$  ratio of projected susceptibility component ratio onto the image plane is defined as:

$$R = \frac{|\chi_{zzz}^{(2)}|}{|\chi_{zxx}^{(2)}|} \cos^2 \alpha + 3 \sin^2 \alpha. \quad (2)$$

The magnitude of the chiral susceptibility component ratio,  $C$  is expressed as:

$$C = \frac{|\chi_{xyz}^{(2)}|}{|\chi_{zxx}^{(2)}|} \sin \alpha, \quad (3)$$

where  $\alpha$  corresponds to the out-of-image-plane tilt angle of the tissue fibers. Note that in general  $C$  ratio is complex valued and can be written as  $Ce^{i\Delta_{xyz}}$ . This is due to the fact that the  $\chi_{xyz}^{(2)}$  susceptibility component is assumed to be complex with a  $\Delta_{xyz}$  phase retardancy between achiral and chiral susceptibility tensor components [38, 43]. We also assume that  $|\chi_{zxx}| \approx |\chi_{xxz}|$  [38] due to nonresonant conditions for collagen at 1030 nm laser radiation wavelength.

## 2.2 | Stokes polarimetric parameters with linear incident polarizations

When incident linear polarizations are employed, the SHG linear dichroism (SHG<sub>LD</sub>), which depends on the in-plane orientation angle  $\delta$  of the fibrillar structures, can be readily obtained. The angle  $\delta$  is defined from the  $Z$ -axis that coincides with the vertical direction of the images.

The SHG<sub>LD</sub> is defined as:

$$\text{SHG}_{\text{LD}} = 2 \frac{s_0^{\text{HLP}} - s_0^{\text{VLP}}}{s_0^{\text{HLP}} + s_0^{\text{VLP}}} = \frac{2\sqrt{3}M_{0,3}}{\sqrt{2}M_{0,1} + M_{0,2}}. \quad (4)$$

Furthermore, we can relate SHG<sub>LD</sub> to the  $R$  and  $C$  ratios,  $\delta$  angle and phase shift  $\Delta_{xyz}$ . The SHG<sub>LD</sub> numerator can be then expressed as follows:

$$\text{SHG}_{\text{LD,numerator}} = 8(- (R^2 - 1 + 4C^2) \cos 2\delta + 2(R - 1)C \cos \Delta_{xyz} \sin 2\delta), \quad (5)$$

and the denominator can be expressed as:

$$\text{SHG}_{\text{LD,denominator}} = (R - 3)(R + 1) \cos 4\delta - 4(R - 3)C \cos \Delta_{xyz} \sin 4\delta + (3R^2 + 2R + 7) + 16C^2. \quad (6)$$

Equations (5) and (6) show that the signal is modulated with  $\cos 2\delta$  and  $\cos 4\delta$  functions, respectively, and depending on the sign of  $C \cos \Delta_{xyz}$ , the phase of the

modulation shifts slightly to the negative or positive value. The  $C$  ratio scales with  $\cos \Delta_{xyz}$  due to the linear laser beam polarization used in the measurements.

Similarly, when incident and outgoing linear polarizations are employed, the linear anisotropy of linear dichroism for second harmonic LA<sub>LD</sub> can be obtained. The LA<sub>LD</sub> is defined as:

$$\text{LA}_{\text{LD}} = 2 \frac{s_1^{\text{HLP}} - s_1^{\text{VLP}}}{s_0^{\text{HLP}} + s_0^{\text{VLP}}} = \frac{2\sqrt{3}M_{1,3}}{\sqrt{2}M_{0,1} + M_{0,2}}, \quad (7)$$

and in terms of  $R$  and  $C$  ratios,  $\delta$  and phase shift  $\Delta_{xyz}$ , the numerator of LA<sub>LD</sub> is:

$$\begin{aligned} \text{LA}_{\text{LD,numerator}} &= 4((R - 3)(R + 1) \cos 4\delta \\ &\quad + 2(R - 3)C \cos \Delta_{xyz} \sin 4\delta \\ &\quad + (R + 1)^2 - 8C^2). \end{aligned} \quad (8)$$

The denominator for LA<sub>LD</sub> is the same as the denominator for SHG<sub>LD</sub> expressed in Equation (6). The LA<sub>LD</sub> signal is modulated with  $\cos 4\delta$  dependency. There is also a significant phase shift of the modulated component, which depends on the sign of  $C \cos \Delta_{xyz}$ .

If linear polarizations are used to generate SHG and the signal is subjected to a polarization state analyzer (PSA) with circular polarizations, the circular anisotropy of linear dichroism CA<sub>LD</sub> can be expressed as follows:

$$\text{CA}_{\text{LD}} = 2 \frac{s_3^{\text{HLP}} - s_3^{\text{VLP}}}{s_0^{\text{HLP}} + s_0^{\text{VLP}}} = \frac{2\sqrt{3}M_{3,3}}{\sqrt{2}M_{0,1} + M_{0,2}}. \quad (9)$$

In terms of  $R$  and  $C$  ratios,  $\delta$  and phase shift  $\Delta_{xyz}$ , the CA<sub>LD</sub> numerator is:

$$\text{CA}_{\text{LD,numerator}} = 32RC \sin \Delta_{xyz} \cos 2\delta. \quad (10)$$

Moreover, the denominator for CA<sub>LD</sub> is the same as the denominator for SHG<sub>LD</sub> expressed in Equation (6). The CA<sub>LD</sub> signal is modulated with periodicity of  $2\delta$ , and also denominator is modulated by  $4\delta$ . The sign and the magnitude of the CA<sub>LD</sub> function depends on  $R$  and  $C \sin \Delta_{xyz}$ .

## 2.3 | Stokes polarimetric parameters with circular incident polarizations

Circular incident polarizations can be used with the polarization state generator (PSG) to obtain different polarimetric parameters. Total SHG signal intensity can be detected, and

either linear or circular polarizations can be employed for the PSA. The polarimetric parameter of SHG circular dichroism (SHG<sub>CD</sub>) is defined as [40, 41, 44]:

$$\text{SHG}_{\text{CD}} = 2 \frac{s_0^{\text{LCP}} - s_0^{\text{RCP}}}{s_0^{\text{LCP}} + s_0^{\text{RCP}}} = 4 \frac{M_{0,9} - M_{0,8}}{\sqrt{6}M_{0,1} - \sqrt{3}M_{0,2} - M_{0,4}}. \quad (11)$$

The SHG<sub>CD</sub> can be expressed in terms of the  $R$  and  $C$  ratios, and the phase shift  $\Delta_{\text{xyz}}$ , as follows:

$$\text{SHG}_{\text{CD}} = \frac{-8C \sin \Delta_{\text{xyz}} (R+1)}{(R-1)^2 + 4(2C^2 + 1)}. \quad (12)$$

It can be seen that SHG<sub>CD</sub> depends on  $C \sin \Delta_{\text{xyz}}$  and that it can flip its sign depending on the alpha orientation angle (see Equation 3). The SHG<sub>CD</sub> also depends on the relative phase shift  $\Delta_{\text{xyz}}$  when nonlocal interaction is assumed [43]. The  $C$  ratio scales with  $\sin \Delta_{\text{xyz}}$  due to the use of circularly polarized laser beam in the measurement. The SHG<sub>CD</sub> also depends on the  $R$  ratio, however, the sign of SHG<sub>CD</sub> will not flip due to  $R$  dependence on the fiber tilt angle  $\alpha$  (see Equation 2). Hence, changing the tilt angle  $\alpha$  from positive to negative values, flips the sign of SHG<sub>CD</sub>.

If the SHG signal generated by a circularly polarized laser beam is subjected to a PSA with linear polarizations, the linear anisotropy of circular dichroism (LA<sub>CD</sub>) is obtained:

$$\text{LA}_{\text{CD}} = 2 \frac{s_1^{\text{LCP}} - s_1^{\text{RCP}}}{s_0^{\text{LCP}} + s_0^{\text{RCP}}} = 4 \frac{M_{1,9} - M_{1,8}}{\sqrt{6}M_{0,1} - \sqrt{3}M_{0,2} - M_{0,4}}. \quad (13)$$

The expression in terms of  $R$  and  $C$  susceptibility ratios,  $\delta$  and phase shift  $\Delta_{\text{xyz}}$  is:

$$\text{LA}_{\text{CD}} = \frac{8C \sin \Delta_{\text{xyz}} (R-3) \cos 2\delta}{(R-1)^2 + 4(2C^2 + 1)}. \quad (14)$$

The equation of LA<sub>CD</sub> shows the  $2\delta$  modulation of the signal. The amplitude and sign of LA<sub>CD</sub> directly depends on  $C \sin \Delta_{\text{xyz}}$ . Moreover, LA<sub>CD</sub> approaches 0, when the  $R$  ratio value is close to 3.

Analogously, the circular anisotropy of circular dichroism of SHG (CA<sub>CD</sub>) is defined as:

$$\text{CA}_{\text{CD}} = 2 \frac{s_3^{\text{LCP}} - s_3^{\text{RCP}}}{s_0^{\text{LCP}} + s_0^{\text{RCP}}} = 4 \frac{M_{3,9} - M_{3,8}}{\sqrt{6}M_{0,1} - \sqrt{3}M_{0,2} - M_{0,4}}. \quad (15)$$

The CA<sub>CD</sub> can also be expressed in terms of  $R$  and  $C$  ratios:

$$\text{CA}_{\text{CD}} = \frac{8((R-1) + 2C^2)}{(R-1)^2 + 4(2C^2 + 1)}. \quad (16)$$

The out-of-image-plane angle  $\alpha$  is explicitly included in the  $R$  and  $C$  ratios. Moreover,  $C$  ratio has a quadratic dependence, and when assumed to be small, it can be dropped out of the equation. CA<sub>CD</sub> expression can be conveniently used for calculating  $R$  ratio.

## 2.4 | Ultrastructural parameters obtained from polarimetric Stokes measurements of SHG

Often, the objective of polarimetric experiments is to obtain the ultrastructural parameters, for example, the achiral and chiral susceptibility ratios  $R$  and  $C$ , respectively, and the cylindrical axis orientation angle  $\delta$ . The  $R$  ratio can be expressed using CA<sub>CD</sub> [40]:

$$\begin{aligned} R &= 1 + \frac{4}{\text{CA}_{\text{CD}}} \pm 2 \sqrt{\frac{4}{\text{CA}_{\text{CD}}^2} - 1 - 2C^2 + \frac{4C^2}{\text{CA}_{\text{CD}}}} \\ &= 1 + \frac{4}{\text{CA}_{\text{CD}}} \pm 2 \sqrt{\frac{4}{\text{CA}_{\text{CD}}^2} - 1}, \end{aligned} \quad (17)$$

and the physically adequate range of  $R$  defines the correct sign. If  $C^2$  is assumed to be small, where  $(R-1) \gg 2C^2$ , the approximate  $R$  ratio can be calculated. This equation can be used for calculating collagen  $R$  ratio, when  $C$  ratio is  $\leq 0.1$ .

The  $C \sin \Delta_{\text{xyz}}$  can be calculated from SHG<sub>CD</sub> measurements by knowing  $R$  and assuming that  $C^2$  is small:

$$C \sin \Delta_{\text{xyz}} = \frac{-\text{SHG}_{\text{CD}} ((R-1)^2 + 4)}{8(R+1)}. \quad (18)$$

Notice that SHG<sub>CD</sub> and CA<sub>CD</sub> are independent of the in-plane angle of the fibrils,  $\delta$ .

In addition, we can calculate  $\cos 2\delta$  from SHG<sub>LD</sub> and LA<sub>LD</sub>, assuming  $(R+1) \gg 2C \cos \Delta_{\text{xyz}}$ :

$$\cos 2\delta = \frac{-2k_3 - \sqrt{4k_3^2 - 8k_1(k_2k_1 - 1)}}{4k_1}, \quad (19)$$

where

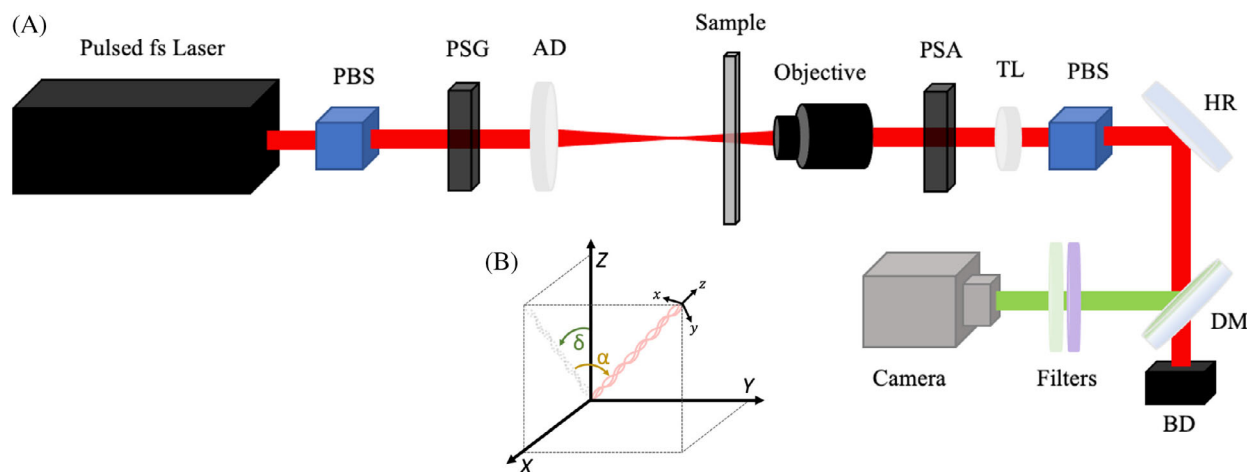


**FIGURE 1** The outline of wide-field polarimetric nonlinear microscopy setup (A). The laser beam is passed through the polarization state generator containing polarizing beam splitter (PBS) and liquid crystal variable retarder (LCVR) that creates an appropriate polarization state for the fundamental beam. A 75 mm focal length achromatic doublet focuses the beam just before the sample. The second harmonic generation (SHG) or MPF and fundamental beams are collected by the objective. The polarization state analyzer containing LCVR and a second PBS probe different polarization states of the SHG or MPF signal. The tube lens (TL) projects the beam onto the camera. The beam passes high reflection mirror (HR), dichroic mirror (DM), and appropriate filters. The separated laser beam from the DM is directed to the beam dump (BD). The microscope part of the setup is built vertically in upright configuration for convenient imaging of biological samples. Schematic of the frame of reference of a sample fiber  $xyz$  with respect to the frame of reference of the laboratory  $XYZ$  (B). The  $\alpha$  and  $\delta$  angles correspond to the out-of-image-plane and in-image-plane orientation of the sample, respectively.

$$k_1 = \frac{\text{SHG}_{\text{LD}}}{\text{LA}_{\text{LD}}}, k_2 = \frac{R+1}{R-3}, k_3 = \frac{R-1}{R-3}. \quad (20)$$

We can also obtain the in-plane orientation independent average SHG intensity when the incident circularly polarized states are employed. The intensity is expressed in terms of Stokes vector components, namely:

$$I_{\text{SHG}} = \frac{1}{2} (s_0^{\text{LCP}} + s_0^{\text{RCP}}). \quad (21)$$

### 3 | MATERIALS AND METHODS

#### 3.1 | Wide-field polarimetric nonlinear optical microscope

A previously described wide-field polarimetric microscope was used [16]. The setup outline is presented in Figure 1. A high power amplified femtosecond laser (PHAROS PH1-10; Light Conversion) was used for a large area wide-field illumination. The laser wavelength was 1030 nm, with a pulse width of 184 fs. The 1030 nm wavelength excitation provides eosin fluorescence and SHG image contrasts. The laser beam was coupled to the microscope. The microscope contained a PSG comprised of a polarizing cube and a liquid crystal retarder (LCC1423-B; Thorlabs). A 75 mm focal length lens was

used to focus the beam for wide-field sample illumination. The samples were placed above the focal plane. The illumination area was adjusted by translating the lens axially. The SHG signal radiated in forward direction was imaged with  $\times 20$  0.5 numerical aperture air objective lens (Carl Zeiss). The PSA comprised of a liquid crystal retarder (LCC1423-A; Thorlabs) was placed after the objective. The SHG signal then passed through a tube lens, a linear polarizing cube, a dichroic mirror, and two filters (BG39 Schott glass filter, and 515 nm 10 nm bandwidth interference filter). Two-photon excitation fluorescence of eosin peaks at 557 nm wavelength [6], and the filters for SHG ensured no leakage of eosin fluorescence and fundamental light. The filtered SHG signal was projected onto a sCMOS camera (Hamamatsu Orca-Flash 4), resulting in  $700 \mu\text{m} \times 700 \mu\text{m}$  imaged sample area, limited by the camera chip area. The transmission efficiency for the illumination path in the microscope was found to be  $\sim 93\%$ . The SHG transmission efficiency from the sample to the detector was 50%. Significant depolarization was not observed from the objective lens and the liquid crystal variable retarders.

A Z-cut quartz plate and a 100- $\mu\text{m}$ -thick lithium triborate crystal attached to an electron microscope gold grid were used for the calibration of polarization setup. The power measured at the end of a circular isolator is used in order to measure the liquid crystal retarder polarization effect on the beam. At the maxima and minima of

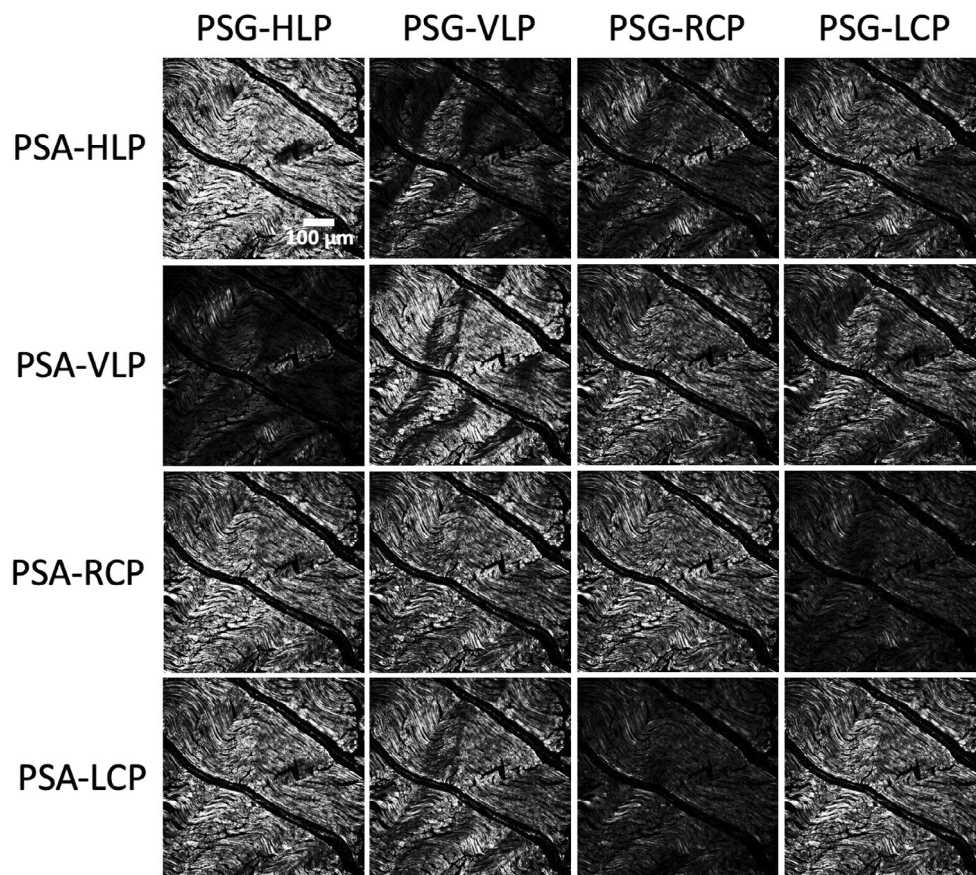


**FIGURE 2** An example of longitudinally cut rat tail tendon second harmonic generation images at 16 different combinations of polarization states, measured for the polarimetric parameters calculation. The horizontally and vertically linearly polarized (HLP and VLP, respectively) and right and left circularly polarized (RCP and LCP, respectively) states were used for polarization state generator (PSG) and polarization state analyzer (PSA).

the power measured, we will have a perfectly circular and linear polarized beams, respectively. The image produced by the lithium triborate crystal with the gold grid was analyzed and the intensity profile showed a Gaussian-like distribution. The illumination area was adjusted to the FWHM of the distribution by axially translating the illumination lens.

### 3.2 | Sample preparation

The tendon was harvested from a healthy rat euthanized after an unrelated study with approval of the Animal Care Committee of the University Health Network, Toronto, Canada. The tendon was formalin fixed and cut approximately along the tendon axis (longitudinal cut) and at  $\alpha = 45^\circ$  (oblique cut). The samples were embedded in paraffin, cut into 5- $\mu\text{m}$ -thick sections deparaffinated and stained with hematoxylin and eosin (H&E), according to a standard histopathology slide preparation procedure [45].

The human nonsmall cell lung carcinoma tissue was obtained with written informed patient consent, and the study was approved by the Research Ethics Board of University Health Network, Toronto, Canada, in accordance with relevant guidelines and regulations and in

compliance with the tenets of the Declaration of Helsinki. The sample was formalin fixed and embedded in paraffin blocks. The sample was cut into 5- $\mu\text{m}$ -thick sections and mounted on a glass slide. The tissue was stained with H&E and imaged with a bright-field microscope scanner (Aperio Whole Slide Scanner; Leica Biosystems) for histopathology investigations. The regions of interest encompassing nonsmall cell carcinoma were selected by expert pathologists (E.Ž. and M.T.) to investigate polarimetric and ultrastructural parameters.

## 4 | RESULTS AND DISCUSSIONS

### 4.1 | Wide-field polarimetric SHG imaging of H&E stained rat tail tendon

Large area polarimetric imaging of H&E stained histology tissue sections is achieved without substantial fluorescence bleaching and SHG signal increase using 2  $\text{mJ}/\text{cm}^2$  pulse energy density and 366 kHz pulse repetition rate resulting in average power of 3.3 W at the microscope entrance [17]. A 1-s frame integration time was used to achieve the images with the signal to noise ratio of 3 (for the lowest intensity images at certain PSG and PSA configurations). The 16 different combinations

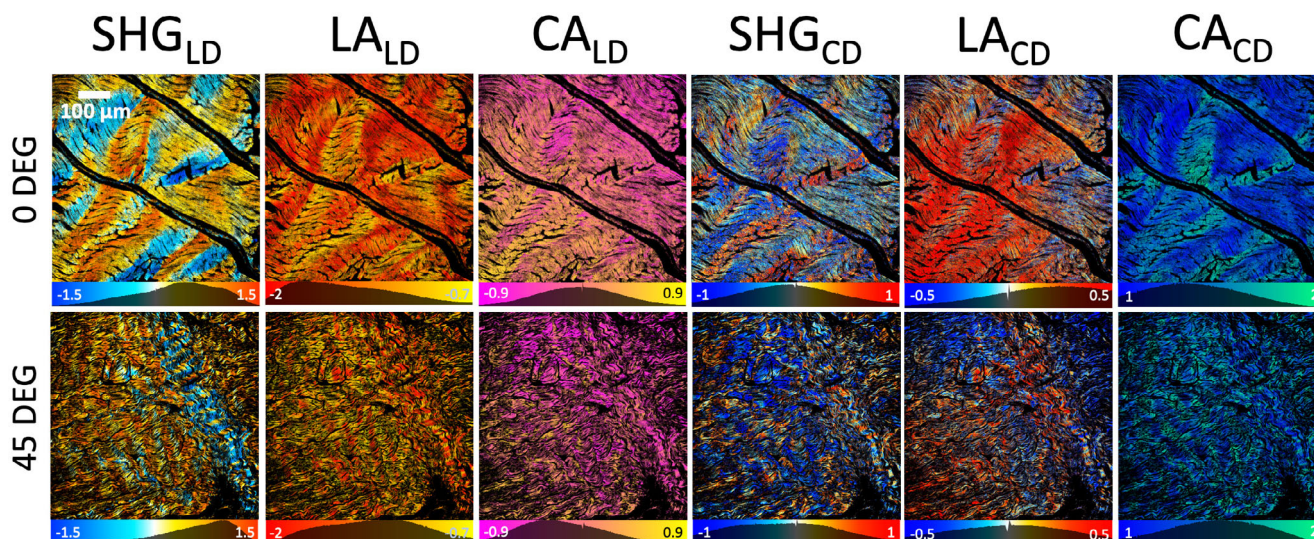


**FIGURE 3** Polarimetric parameters for collagenous tissue in rat tail tendon. First row corresponds to a longitudinal cut with  $\alpha$  close to  $0^\circ$ . The second row corresponds to a  $45^\circ$  cut of rat tail tendon. Images of each polarimetric parameter are presented in separate columns with labels on the column top.

of incident and outgoing polarization states were used. The total exposure time of the same sample area was 16 s, leading to negligible bleaching of eosin fluorescence and virtually no photoinduced increase of SHG signal [17]. One liquid crystal variable retarder was used for the PSG and also one liquid crystal variable retarder was employed for the analyzer. This ensured quick and easy calibration of the liquid crystals. The intensity images of the same sample area at various polarization states are shown in Figure 2. The polarization states of PSG are given in the columns and polarization states of PSA are given in the rows of Figure 2. Different areas of the sample respond differently to various incoming and outgoing polarization states. A large effect can be seen involving different circular states for PSG and PSA. The SHG images at different polarization states are used to calculate the resulting Stokes vector components maps and then to calculate the maps of polarimetric parameters.

#### 4.2 | Polarimetric parameters at different cut angles for the rat tail tendon

The maps of polarimetric parameters of  $\text{SHG}_{\text{LD}}$ ,  $\text{LA}_{\text{LD}}$ , and  $\text{CA}_{\text{LD}}$ , as well as  $\text{SHG}_{\text{CD}}$ ,  $\text{LA}_{\text{CD}}$ , and  $\text{CA}_{\text{CD}}$  are presented in Figure 3. The maps are calculated from the SHG Stokes vector elements using Equations (4), (7), (9), (11), (13), and (15), respectively. Stokes vector elements are calculated from the intensity images at different PSG and PSA states (see Figure 2). The images of polarimetric parameters are calculated directly from the measured intensity images without assuming any susceptibility

tensor symmetries. Therefore, the polarimetric images are obtained quickly from the raw data without any fitting requirement. For interpretation of the images of polarimetric parameters, it is informative to assume  $C6$  symmetry with a complex valued chiral susceptibility component and use Equations (5), (8), and (10) for  $\text{SHG}_{\text{LD}}$ ,  $\text{LA}_{\text{LD}}$ , and  $\text{CA}_{\text{LD}}$ , respectively, and Equations (12), (14), and (16) for  $\text{SHG}_{\text{CD}}$ ,  $\text{LA}_{\text{CD}}$ , and  $\text{CA}_{\text{CD}}$ , respectively.

The images of  $\text{SHG}_{\text{LD}}$  highlight the in-image-plane fiber orientation (Figure 3 first column). The  $\text{SHG}_{\text{LD}}$  has  $2\delta$  modulation of the values that reveal fiber orientation ranging from vertical at  $\delta = 0^\circ$  to horizontal at  $\delta = \pm 90^\circ$ . The deduced orientation angle is slightly modified compared to the actual fiber orientation due to presence of complex valued chiral susceptibility ratio (Equation (5)). For a well aligned structure of tendon cut longitudinally, the  $\text{SHG}_{\text{LD}}$  values follow closely the orientation of collagen fibers. For the oblique cut, the fiber orientations are not clearly visible, but red pixel color indicates dominant horizontal orientation, and only a few strands are oriented toward vertical direction as indicated by the blue color of the pixels (Figure 2, lower row, first panel).

The  $\text{LA}_{\text{LD}}$  has  $4\delta$  modulation and carries fiber orientation information. The  $\text{LA}_{\text{LD}}$  values are mostly negative for collagen (see Equation (8)). The  $\text{SHG}_{\text{LD}}$  and  $\text{LA}_{\text{LD}}$  are used to extract the fiber orientation  $\cos 2\delta$ , as will be shown in the next section.

The  $\text{CA}_{\text{LD}}$ , parameter has  $2\delta$  modulation, therefore it is sensitive to fiber orientation. However,  $\text{CA}_{\text{LD}}$  has strong dependence on  $C$  ratio and  $R$  ratio, and, in turn, on the tilt angle  $\alpha$  out of the image plane. Therefore, the

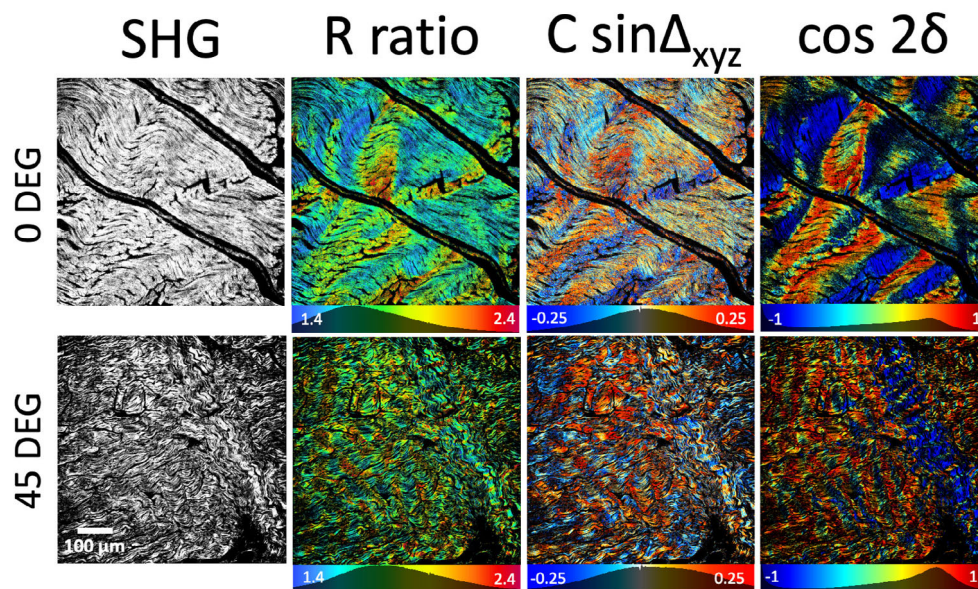


**FIGURE 4** Maps of second harmonic generation intensity and ultrastructure parameters  $R$ ,  $C \sin \Delta_{xyz}$ , and orientation  $\cos 2\delta$  (respective columns) for collagen tissue in rat tail tendon. The upper row corresponds to a longitudinal cut with  $\alpha$  close to  $0^\circ$ , and the lower row corresponds to a  $45^\circ$  cut of rat tail tendon. The ultrastructure parameters are calculated from polarimetric parameters shown in Figure 3.

values of  $CA_{LD}$  have to be interpreted with caution, but this parameter can be employed in combination with other polarimetric parameters to extract ultrastructural information.

Polarimetric parameters with incident circular polarization states provide in-image-plane orientation free assessment of the fibers. The forth column of Figure 3 shows  $SHG_{CD}$ , which depends on the  $C$  ratio. The  $\Delta_{xyz}$  influences the chiral susceptibility component that has complex values with respect to the achiral susceptibility components that are real valued [38].  $C$  ratio depends on the out-of-image-plane tilt angle  $\alpha$  of the fibrils. The waviness of the collagen out and again into the image plane for the tendon longitudinal cut is nicely reflected in the  $SHG_{CD}$  image (Figure 3, first row). The  $SHG_{CD}$  is very informative at the oblique angle cut (Figure 3 second row). The distribution of the  $SHG_{CD}$  values becomes much broader for oblique cut compared to the longitudinal cut due to  $\alpha$  dependence (Equation 3). The oblique cut image reveals islands of collagen oriented with opposite polarity, feature observed previously [37, 38].  $SHG_{CD}$  is a very robust and quick measurement to assess collagen polarity, and can be performed with a dual or a single shot polarimetric measurement [40].

The  $LA_{CD}$  polarimetric parameter images show in-image-plane fiber orientation dependence  $2\delta$  (Figure 3 fifth column). In addition  $LA_{CD}$  has strong  $C$  ratio and  $R$  ratio dependence (Equation 13). Therefore, the interpretation of  $LA_{CD}$  images is complex due to simultaneous influence of several factors. The numerators in expressions of  $CA_{LD}$  and  $LA_{CD}$  (Equations 10 and 14) have the same dependence on  $2\delta$  and  $C$  ratio, and similar dependence on  $R$  ratio, therefore the images of  $CA_{LD}$  and  $LA_{CD}$  reveal similar features (compare Figure 3, third and fifth column).

The  $CA_{CD}$  parameter is independent of the in-image-plane fiber orientation and depends on the  $R$  and  $C^2$ . The  $CA_{CD}$  parameter is particularly well suited for calculating  $R$  ratio (see Equation 17), as will be shown in the next section.  $CA_{CD}$  peak value of the distribution for longitudinal cut tendon is smaller than for the oblique cut, demonstrating the dependence of  $CA_{CD}$  on tilt angle  $\alpha$ , according to Equation (2).

The polarimetric parameters provide quick assessment of the tissue collagen ultrastructure directly from the measurements without fitting of the imaged data. The polarimetric parameters can be further employed to calculate the ultrastructure parameters.

### 4.3 | Ultrastructure parameters at different cut angles for the rat tail tendon

The maps of ultrastructure parameters (Figure 4) can be calculated from the polarimetric parameters using Equations (17)–(19) and (21). The ultrastructural parameters  $R$  ratio,  $C \sin \Delta_{xyz}$ , and  $\cos 2\delta$  characterize the collagen fibrils organization in the focal volume below the diffraction limited resolution. The two rows of images of the ultrastructure parameters are given in Figure 4 for comparison of longitudinal cut and oblique cut  $\sim 45^\circ$  of the tendon.  $R$  ratio is calculated from  $CA_{CD}$  using Equation (17). It slightly varies along the length of longitudinally cut tendon reflecting the out of image plane waviness of the structure.  $R$  ratio increases for the oblique angle cut (see  $R$  ratio image histograms in Figure 4) due to  $\alpha$  dependence in accordance with Equation (2). The large area imaging of  $R$  ratio, which reflects the ultrastructure of collagen, can be obtained quickly by



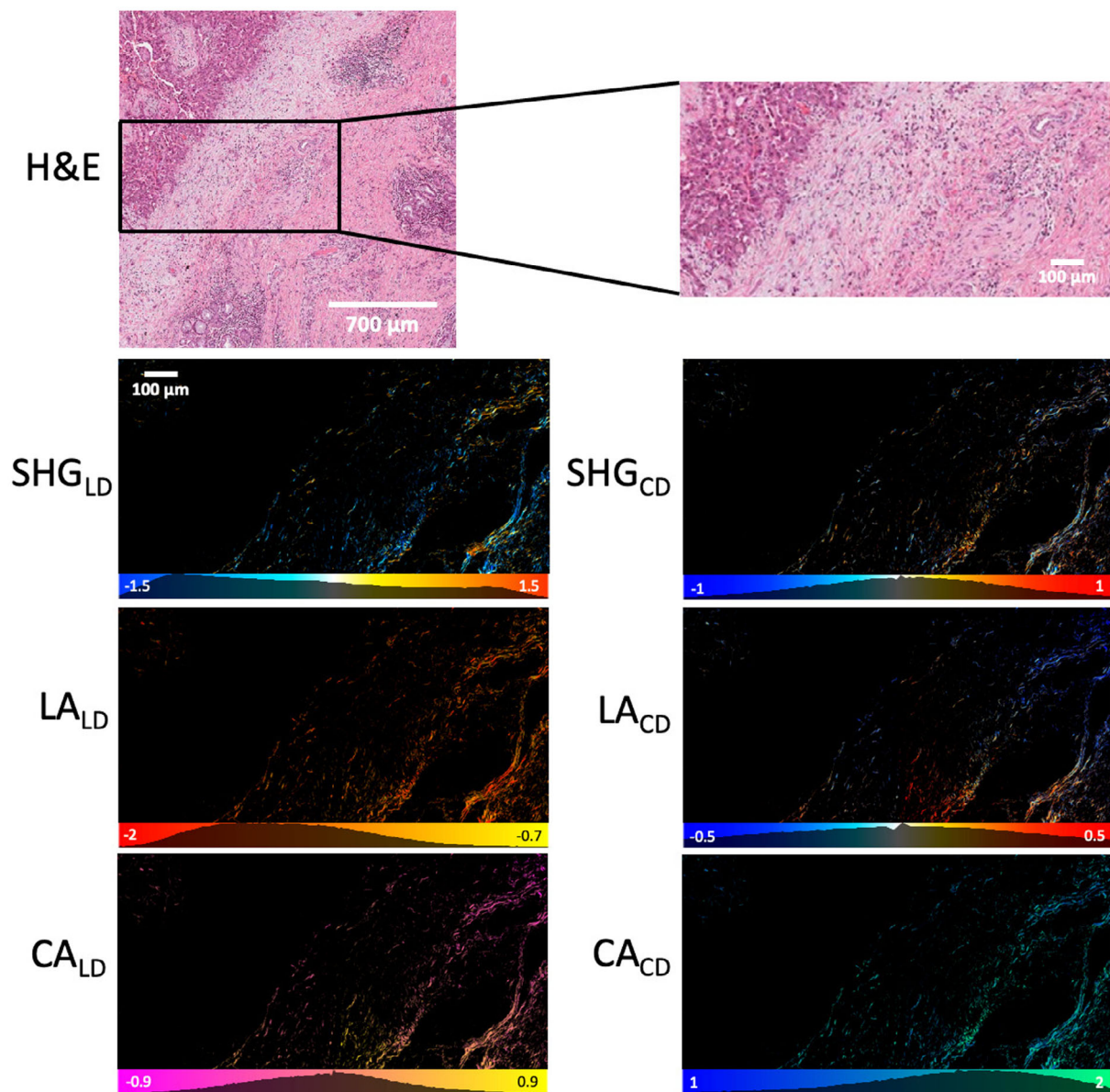


**FIGURE 5** Images of polarimetric parameters for a nonsmall cell lung carcinoma tumor margin of hematoxylin and eosin (H&E) stained tissue section. Images of each polarimetric parameter are presented with labels near each image. The color bars contain pixel value distribution for a corresponding image. In addition, the bright-field images of H&E stained tissue are included for reference.

imaging with wide-field Stokes polarimetric microscopy and calculating the values without data fitting. The out-of-plane orientation information is closely related to  $R$  ratio. This comes from the tensor rotation between laboratory and molecular susceptibilities. If  $C_6$  symmetry of the collagen fibers is assumed, and the fibers are aligned parallel to each other in the focal volume, the molecular susceptibility ratios and  $\alpha$  are related to  $R$  ratio according to Equation (2).

The  $C \sin \Delta_{xyz}$  map (Figure 4) reflects the out of image plane orientation of collagen fibers according to Equation (3). The  $C \sin \Delta_{xyz}$  map is similar to  $SHG_{CD}$  shown in Figure 3, due to the close relation expressed in

Equation (18). The longitudinal map of  $C \sin \Delta_{xyz}$  (Figure 4) shows fiber tilt angle deviations from the image plane reflecting waviness of collagen fibers in the tendon. The oblique cut shows blue and red areas reflecting different polarity of collagen strands in the tendon. The  $C \sin \Delta_{xyz}$  value histogram for oblique cut is broader compared to the longitudinal cut due to larger  $\alpha$  angle values.

The  $\cos 2\delta$  map shows a very clear representation of in-image-plane orientation of the collagen fibers. For the longitudinal cut (upper row, Figure 4) the fiber in-image-plane orientation follows a wave pattern; for the oblique cut (lower row, Figure 4), the collagenous tissue exhibits

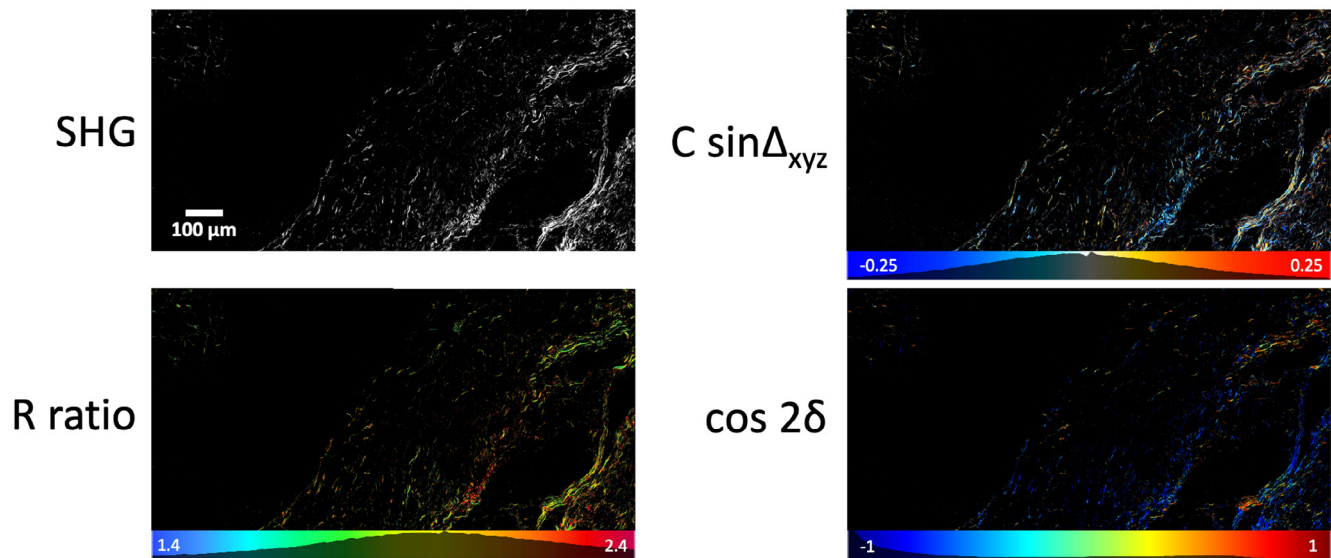


**FIGURE 6** Nonsmall cell lung carcinoma tumor margin images for second harmonic generation intensity and ultrastructure parameters  $R$ ,  $C \sin \Delta_{xyz}$ , and orientation  $\cos 2\delta$ . The ultrastructure parameters are calculated from polarimetric parameters shown in Figure 5.

homogeneous directionality, with the exception of one cluster of fibers that are organized perpendicularly.

The reduced polarimetric measurements of tissue sections with wide-field microscopy enable large area ultrastructural assessment of collagen, which extends the utility of SHG imaging for various applications including cancer diagnostics [31, 46] and monitoring live dynamics, for example, in contracting muscle fibers [18].

#### 4.4 | Lung tumor margin imaging with Stokes polarimetric microscopy

Wide-field SHG Stokes polarimetric microscopy and direct calculations of ultrastructure parameters (without fitting) enable quick large area imaging, which is required for whole-slide digital pathology. We present tumor margin images of nonsmall cell lung carcinoma. The image area was  $0.7 \text{ mm} \times 1.4 \text{ mm}$ . The maps of polarimetric parameters, namely,  $\text{SHG}_{LD}$ ,  $\text{LA}_{LD}$ ,  $\text{CA}_{LD}$ ,  $\text{SHG}_{CD}$ ,  $\text{LA}_{CD}$ , and  $\text{CA}_{CD}$  are presented in Figure 5. The images are obtained in the same way as previously described for the rat tail tendon (Figure 3). The images of ultrastructural parameters of the lung tumor margin are presented in Figure 6. The ultrastructure images are obtained in the same way as the rat tail tendon images from Figure 4. The lung tumor margin images show that tissue exhibits much less SHG intensity compared to the tendon structure, which is consistent with the previous observations that SHG intensity decreases around the lung tumor and the signal is very low within the tumor area [16, 46]. The comparison of bright-field (Figure 5) and SHG images (Figure 6) shows that a brighter layer

surrounding the tumor body in white-light image corresponds to a layer of very low SHG signal with low SHG pixel density. A more distant area from the tumor shows SHG signal increase and larger SHG pixel density, however, SHG signal of the collagen is much weaker than for the tendon tissue. The reduced SHG intensity can be attributed to disordered collagen [16, 46].

The polarimetric parameters (Figure 5) give ample information about the tissue collagen.  $\text{SHG}_{LD}$  image provides with approximate in-image-plane orientation information of collagen strands. The tumor margin is oriented at about  $20^\circ$  from the vertical. The  $\text{SHG}_{LD}$  value distribution shows that collagen is predominantly oriented toward vertical, that is, along the tumor margin (Figure 5).  $\text{LA}_{LD}$  has  $4\delta$  modulation and provides collagen fiber orientation information, similar to  $\text{SHG}_{LD}$  (Figure 5). Both  $\text{SHG}_{LD}$  and  $\text{LA}_{LD}$  are used to extract  $\cos 2\delta$  ultrastructural parameter (Figure 6), which also shows that collagen strands are oriented predominantly along the tumor margin. Collagen fiber orientation may play a role in metastasis of tumor cells [47].

$\text{CA}_{LD}$  and  $\text{LA}_{CD}$  are modulated by  $\sin 2\delta$ , but also have a linear dependence on  $R$  and  $C$  ratios, therefore, the map interpretation of these polarimetric parameters is ambiguous.  $\text{CA}_{LD}$  and  $\text{LA}_{CD}$  can be used with other parameters to extract the ultrastructural information about the tissue collagen.

$\text{SHG}_{CD}$  polarimetric parameter provides  $\delta$  orientation independent assessment of the tissue and strongly depends on  $C$  ratio, and also on  $R$  ratio.  $\text{SHG}_{CD}$  is used to extract  $C \sin \Delta_{xyz}$  maps with known  $R$  ratios (see Equation 18). The  $C$  ratio has  $\sin \alpha$  dependence, therefore change in the sign of  $\text{SHG}_{CD}$  indicates tilt orientation

change of collagen fibers from the out-of-image-plane to the into-image-plane configuration. Therefore, sign of  $\text{SHG}_{\text{CD}}$  indicates polarity of collagen strands with respect to the image plane. The lung tumor margin has mostly homogeneous bipolar distribution of collagen, and only some areas show preferentially positive or negative polarity (see  $\text{SHG}_{\text{CD}}$  image in Figure 5, and also  $C\sin\Delta_{\text{xyz}}$  image in Figure 6).

$\text{CA}_{\text{CD}}$  polarimetric parameter (Figure 5) depends mostly on  $R$  ratio, and when assuming that  $(R - 1) \gg 2C^2$ , the  $R$  ratio map can be obtained (Figure 6).  $\text{CA}_{\text{CD}}$  shows rather homogeneous distribution with minor clustering of values along the tumor margin (Figure 5). The calculated  $R$  ratio map shows corresponding homogeneous distribution of values with small clustering along the tumor margin (Figure 6). The  $R$  ratio distribution maximum is around 2.03 with a standard deviation of 0.36, which is consistent with the previous investigations of lung tumor tissue [46]. This is in sharp contrast with the  $R$  ratio of tendon collagen cut at  $0^\circ$  ( $1.72 \pm 0.24$ ) and  $45^\circ$  ( $1.84 \pm 0.27$ ).

## 5 | CONCLUSIONS

The wide-field polarimetric SHG microscopy imaging can be used for high-throughput comparative assessment of collagen organization in histopathology samples. The images of Stokes parameters can be obtained from polarimetric measurements with both linear and circular incident and outgoing polarizations. The Stokes parameters are used to calculate polarimetric parameters, namely,  $\text{SHG}_{\text{LD}}$ ,  $\text{LA}_{\text{LD}}$ , and  $\text{CA}_{\text{LD}}$ , as well as  $\text{SHG}_{\text{CD}}$ ,  $\text{LA}_{\text{CD}}$ , and  $\text{CA}_{\text{CD}}$ . In turn, the ultrastructure parameters  $R$ ,  $C\sin\Delta_{\text{xyz}}$ , and  $\cos 2\delta$  can be calculated from the polarimetric parameters without fitting. The ultrastructure parameters, as well as polarimetric parameters provide with a rapid way of characterizing ultrastructure of collagen in the tissue for histopathology investigations.

A lung tumor margin imaging is presented using Stokes SHG polarimetric microscopy. The maps of polarimetric and ultrastructure parameters were calculated.  $R$  ratio map of the tumor margin (Figure 6) shows rather homogeneous values over the image area, with the peak of the distribution around 2.03, which is consistent with the previous studies [46]. The  $C\sin\Delta_{\text{x,y,z}}$  shows homogeneously distributed collagen polarity along the tumor margin with some clustering islands of positive and negative values. The collagen orientation distribution provided by the  $\cos 2\delta$  map (Figure 6) shows that the strands are oriented predominantly along the tumor margin for this area of lung tissue. The  $R$  and  $C$  as well as  $\delta$  maps enable to assess the ultrastructure of collagen for use in

cancer diagnostics. The wide-field SHG Stokes polarimetry opens a possibility for quick whole-slide imaging, and enables to use collagen as a biomarker for cancer diagnostics in nonlinear optical histopathology.

## ACKNOWLEDGMENTS

The authors would like to acknowledge Light Conversion for lending the laser for experiments. The work was supported by Natural Sciences and Engineering Research Council of Canada (NSERC) (RGPIN-2017-06923, DGDND-2017-00099), and the European Regional Development Fund (project No 01.2.2.-LMT-K-718-02-0016) under grant agreement with the Research Council of Lithuania (LMTLT).

## CONFLICT OF INTEREST STATEMENT

The authors declare no conflict of interests.

## DATA AVAILABILITY STATEMENT

The data that support the findings of this study are available from the corresponding author upon reasonable request.

## ORCID

Leonardo Uribe Castaño  <https://orcid.org/0000-0002-0650-5427>

Brian C. Wilson  <https://orcid.org/0000-0001-5543-666X>

## REFERENCES

- [1] S. Roth, I. Freund, *J. Chem. Phys.* **1979**, *70*, 1637.
- [2] I. Freund, M. Deutsch, *Opt. Lett.* **1986**, *11*, 94.
- [3] S.-W. Chu, S.-Y. Chen, G.-W. Chern, T.-H. Tsai, Y.-C. Chen, B.-L. Lin, C.-K. Sun, *Biophys. J.* **2004**, *86*, 3914.
- [4] P. Stoller, K. M. Reiser, P. M. Celliers, A. M. Rubenchik, *Biophys. J.* **2002**, *82*, 3330.
- [5] P. C. Stoller, B.-M. Kim, A. M. Rubenchik, K. M. Reiser, L. B. Da Silva, *J. Biomed. Opt.* **2002**, *7*, 205.
- [6] A. E. Tuer, D. Tokarz, N. Prent, R. Cisek, J. Alami, D. J. Dumont, L. Bakueva, J. A. Rowlands, V. Barzda, *J. Biomed. Opt.* **2010**, *15*, 1.
- [7] F. Tiaho, G. Recher, D. Rouède, *Opt. Express* **2007**, *15*, 12286.
- [8] P. Stoller, P. M. Celliers, K. M. Reiser, A. M. Rubenchik, *Appl. Opt.* **2003**, *42*, 5209.
- [9] S. Brasselet, *Adv. Opt. Photonics* **2011**, *3*, 205.
- [10] O. Masihzadeh, P. Schlup, R. A. Bartels, *Opt. Express* **2010**, *18*, 9840.
- [11] D. R. Smith, D. G. Winters, R. A. Bartels, *Proc. Natl. Acad. Sci. U. S. A.* **2013**, *110*, 18391.
- [12] D. G. Winters, D. R. Smith, P. Schlup, R. A. Bartels, *Biomed. Opt. Express* **2012**, *3*, 2004.
- [13] C. Macias-Romero, M. E. P. Didier, P. Jourdain, P. Marquet, P. Magistretti, O. B. Tarun, V. Zubkovs, A. Radenovic, S. Roke, *Opt. Express* **2014**, *22*, 31102.
- [14] E. Shaffer, C. Moratal, P. Magistretti, P. Marquet, C. Depeursinge, *Opt. Lett.* **2010**, *35*, 4102.
- [15] C. Hu, J. J. Field, V. Kelkar, B. Chiang, K. Wernsing, K. C. Toussaint, R. A. Bartels, G. Popescu, *Nat. Photonics* **2020**, *14*, 564.

- [16] K. Mirsanaye, L. Uribe Castaño, Y. Kamaliddin, A. Golaraei, R. Augulis, L. Kontenis, S. J. Done, E. Žurauskas, V. Stambolic, B. C. Wilson, V. Barzda, *Sci. Rep.* **2022**, *12*, 10290. <https://doi.org/10.1038/s41598-022-13623-1>
- [17] L. U. Castaño, K. Mirsanaye, A. Golaraei, L. Kontenis, S. J. Done, V. Stambolic, M. K. Akens, B. C. Wilson, V. Barzda, *bioRxiv* **2022**, 488489.
- [18] H. Zhao, R. Cisek, A. Karunendiran, D. Tokarz, B. A. Stewart, V. Barzda, *Biomed. Opt. Express* **2019**, *10*, 5130.
- [19] P.-J. Su, W.-L. Chen, Y.-F. Chen, C.-Y. Dong, *Biophys. J.* **2011**, *100*, 2053.
- [20] P.-S. Hu, A. Ghazaryan, V. A. Hovhannisyanyan, S.-J. Chen, Y.-F. Chen, C.-S. Kim, T.-H. Tsai, C.-Y. Dong, *J. Biomed. Opt.* **2012**, *18*, 031102.
- [21] P. Hu, C. Hsueh, P. Su, W. Chen, V. A. Hovhannisyanyan, S. Chen, T. Tsai, C. Dong, *IEEE J. Sel. Top. Quantum Electron.* **2012**, *18*, 1326.
- [22] C. Bonnans, J. Chou, Z. Werb, *Nat. Rev. Mol. Cell Biol.* **2014**, *15*, 786.
- [23] S. M. Pupa, S. Ménard, S. Forti, E. Tagliabue, *J. Cell. Physiol.* **2002**, *192*, 259.
- [24] N. Théret, O. Musso, B. Turlin, D. Lotrian, P. Bioulac-Sage, J.-P. Campion, K. Boudjéma, B. Clément, *Hepatology* **2001**, *34*, 82.
- [25] A. Cho, V. M. Howell, E. K. Colvin, *Front. Oncol.* **2015**, *5*, 245.
- [26] P. P. Provenzano, K. W. Eliceiri, J. M. Campbell, D. R. Inman, J. G. White, P. J. Keely, *BMC Med.* **2006**, *4*, 38.
- [27] P. P. Provenzano, D. R. Inman, K. W. Eliceiri, J. G. Knittel, L. Yan, C. T. Rueden, J. G. White, P. J. Keely, *BMC Med.* **2008**, *6*, 11.
- [28] R. Kalluri, *Nat. Rev. Cancer* **2003**, *3*, 422.
- [29] J. Adur, V. B. Pelegati, A. A. de Thomaz, M. O. Baratti, D. B. Almeida, L. A. L. A. Andrade, F. Bottcher-Luiz, H. F. Carvalho, C. L. Cesar, *PLoS One* **2012**, *7*, e47007.
- [30] A. Brabrand, I. I. Kariuki, M. J. Engstrøm, O. A. Haugen, L. A. Dyrnes, B. O. Åsvold, M. B. Lilledahl, A. M. Bofin, *APMIS* **2015**, *123*, 1.
- [31] A. Golaraei, L. Kontenis, R. Cisek, D. Tokarz, S. J. Done, B. C. Wilson, V. Barzda, *Biomed. Opt. Express* **2016**, *7*, 4054.
- [32] R. Mercatelli, T. Triulzi, F. S. Pavone, R. Orlandi, R. Cicchi, *J. Biophotonics* **2020**, *13*, e202000159.
- [33] V. Tsafas, E. Gavgiotaki, M. Tzardi, E. Tsafa, C. Fotakis, I. Athanassakis, G. Filippidis, *J. Biophotonics* **2020**, *13*, e202000180.
- [34] K. R. Campbell, R. Chaudhary, J. M. Handel, M. S. Patankar, P. J. Campagnola, *J. Biomed. Opt.* **2018**, *23*, 1.
- [35] R. Kumar, K. M. Grønhaug, E. I. Romijn, A. Finnøy, C. L. Davies, J. O. Drogset, M. B. Lilledahl, *J. Biophotonics* **2015**, *8*, 730.
- [36] A. E. Tuer, M. K. Akens, S. Krouglov, D. Sandkuijl, B. C. Wilson, C. M. Whyne, V. Barzda, *Biophys. J.* **2012**, *103*, 2093.
- [37] A. Golaraei, K. Mirsanaye, Y. Ro, S. Krouglov, M. K. Akens, B. C. Wilson, V. Barzda, *J. Biophotonics* **2019**, *12*, e201800241.
- [38] A. Golaraei, L. Kontenis, K. Mirsanaye, S. Krouglov, M. K. Akens, B. C. Wilson, V. Barzda, *Sci. Rep.* **2019**, *9*, 12488.
- [39] K. Mirsanaye, A. Golaraei, F. Habach, E. Žurauskas, J. Venius, R. Rotomskis, V. Barzda, *Biomed. Opt. Express* **2019**, *10*, 5025.
- [40] A. Golaraei, L. Kontenis, A. Karunendiran, B. A. Stewart, V. Barzda, *J. Biophotonics* **2020**, *13*, e201960167.
- [41] M. Samim, S. Krouglov, V. Barzda, *J. Opt. Soc. Am. B* **2015**, *32*, 451.
- [42] M. Samim, S. Krouglov, V. Barzda, *Phys. Rev. A* **2016**, *93*, 013847.
- [43] D. Abramavicius, S. Krouglov, V. Barzda, *Phys. Chem. Chem. Phys.* **2021**, *23*, 20201.
- [44] L. Kontenis, M. Samim, A. Karunendiran, S. Krouglov, B. Stewart, V. Barzda, *Biomed. Opt. Express* **2016**, *7*, 559.
- [45] C. E. Day, *Histopathology Methods and Protocols*, Springer, New York **2014**.
- [46] A. Golaraei, R. Cisek, S. Krouglov, R. Navab, C. Niu, S. Sakashita, K. Yasufuku, M.-S. Tsao, B. C. Wilson, V. Barzda, *Biomed. Opt. Express* **2014**, *5*, 3562.
- [47] A. Keikhosravi, J. S. Bredfeldt, A. K. Sagar, K. W. Eliceiri, in *Quantitative Imaging in Cell Biology: Methods in Cell Biology*, Vol. 123 (Eds: J. C. Waters, T. Wittman), Academic Press, San Diego, CA **2014**, p. 531.

**How to cite this article:** L. Uribe Castaño, K. Mirsanaye, L. Kontenis, S. Krouglov, E. Žurauskas, R. Navab, K. Yasufuku, M.-S. Tsao, M. K. Akens, B. C. Wilson, V. Barzda, *J. Biophotonics* **2023**, *16*(5), e202200284. <https://doi.org/10.1002/jbio.202200284>